



Non-universality of the mass function: dependence on the growth rate and power spectrum shape

Lurdes Ondaro-Mallea,^{1,2★} Raul E. Angulo,^{1,3★} Matteo Zennaro¹ ,¹ Sergio Contreras¹ and Giovanni Aricò^{1,4} 

¹Donostia International Physics Center (DIPC), Manuel Lardizabal Ibilbidea, 4, E-20018 Donostia, Spain

²Universidad Autónoma de Madrid (UAM), C/ Francisco Tomás y Valiente, 7, E-28049 Madrid, Spain

³IKERBASQUE, Basque Foundation for Science, E-48013 Bilbao, Spain

⁴Universidad de Zaragoza, Pedro Cerbuna 12, E-50009 Zaragoza, Spain

Accepted 2021 November 2. Received 2021 October 5; in original form 2021 February 18

ABSTRACT

The abundance of dark matter haloes is one of the key probes of the growth of structure and expansion history of the Universe. Theoretical predictions for this quantity usually assume that, when expressed in a certain form, it depends only on the mass variance of the linear density field. However, cosmological simulations have revealed that this assumption breaks, leading to 10–20 per cent systematic effects. In this paper, we employ a specially designed suite of simulations to further investigate this problem. Specifically, we carry out cosmological N -body simulations where we systematically vary growth history at a fixed linear density field, or vary the power spectrum shape at a fixed growth history. We show that the halo mass function generically depends on these quantities, thus showing a clear signal of non-universality. Most of this effect can be traced back to the way in which the same linear fluctuation grows differently into the non-linear regime depending on details of its assembly history. With these results, we propose a parameterization with explicit dependence on the linear growth rate and power spectrum shape. Using an independent suite of simulations, we show that this fitting function accurately captures the mass function of haloes over cosmologies spanning a vast parameter space, including massive neutrinos and dynamical dark energy. Finally, we employ this tool to improve the accuracy of so-called cosmology-rescaling methods and show they can deliver 2 per cent accurate predictions for the halo mass function over the whole range of currently viable cosmologies.

Key words: methods: statistical – large-scale structure of Universe – cosmology: theory.

1 INTRODUCTION

Collapsed dark matter structures, also known as haloes, offer an important way to constrain fundamental properties of the Universe. The abundance of haloes is sensitive to the growth of structure and the statistics of primordial fluctuations, thus it can be employed to, for instance, constrain the value of cosmic parameters including dark energy and the sum of neutrino masses (Weinberg et al. 2013).

In the next decades, up to hundreds of thousands of haloes with mass above $\sim 10^{13} h^{-1} M_{\odot}$ will be detected by upcoming observational surveys [e.g. *eROSITA* (Hofmann et al. 2017), *EUCLID* (Sartoris et al. 2016), *LSST* (Ivezić et al. 2019), *Simons Observatory* (Ade et al. 2019), *CMB-S4* (Abazajian et al. 2019), and *J-PAS* (Bonoli et al. 2020)]. These future surveys will employ various observables over different wavelengths to identify haloes, such as their Sunyaev–Zeldovich effect, X-ray emission, gravitational lensing, or number of optically detected galaxies. Despite these differences, a necessary ingredient for all such analyses is accurate predictions for the abundance of haloes of a given mass as a function of cosmological parameters.

In the Press–Schechter formalism (Press & Schechter 1974, hereafter PS), the abundance of dark matter haloes of mass M is fundamentally given by the relative abundance of peaks of different types in a Gaussian random field. Specifically, the halo mass function reads

$$\frac{dn}{d \ln M} = -\frac{\rho_b}{M} \frac{d \log \sigma}{d \log M} \nu f(\nu), \quad (1)$$

where ρ_b is the background matter density of the universe; $f(\nu) = \sqrt{2/\pi} \exp(-0.5\nu^2)$; ν is the so-called ‘peak height’ associated to a halo of mass M and is defined as $\nu \equiv \delta_c(z)/\sigma(M, z)$; δ_c is the critical overdensity for collapse; and $\sigma(M, z)$ is the rms linear variance extrapolated at the redshift of interest, z .

In this approach, cosmological parameters and the shape of the power spectrum of fluctuations, $P(k)$, are considered only through modifications to σ :

$$\sigma(R, z) = \frac{D^2(z)}{2\pi} \int_0^{\infty} d^3k P(k) \tilde{W}(k, R)^2, \quad (2)$$

where $D(z)$ is the linear growth factor, and $\tilde{W}(k, R)$ is the Fourier transform of the top-hat window function and $M = \frac{4\pi}{3} \rho_b R^3$. On top of this, $n(M)$ is affected by the cosmological parameters through ρ_b . Since $f(\nu)$ is cosmology-independent, the halo mass function is predicted to be ‘universal’.

* E-mail: lurdes.ondaro@dipc.org (LO-M); reangulo@dipc.org (REA)

The ‘universality’ of the mass function is a key property because it allows for accurate predictions even if PS itself is inaccurate. For instance, if the mass function is universal, a *single* simulation is needed to measure $f(\nu)$, and then use equation (1) to make predictions for any cosmological model. Therefore, computational resources can be focused on accurately measuring $f(\nu)$ using high force and high-mass resolution simulations of large cosmic volumes, rather than requiring large ensembles of simulations spanning the full range of cosmological parameters of interest.

In fact, several early studies found that the PS halo mass function describes only qualitatively the abundance of dark matter haloes in N -body simulations. Motivated by the universality of the mass function, these works have provided much more precise fitting functions for $f(\nu)$, usually employing functional forms inspired by ellipsoidal collapse, but still assuming that all cosmology dependence can be captured through $\sigma(M)$ (e.g. Sheth & Tormen 1999; Jenkins et al. 2001; Sheth & Tormen 2002; Reed et al. 2003; Warren et al. 2006; Reed et al. 2007; Crocce et al. 2010; Bhattacharya et al. 2011; Angulo et al. 2012; Watson et al. 2013; Bocquet et al. 2016; Seppi et al. 2020).

More recently, various authors pointed out and quantified the ‘non-universality’ of the mass function (Tinker et al. 2008; Courtin et al. 2010; Despali et al. 2015; McClintock et al. 2019; Bocquet et al. 2020; Diemer 2020). They have found that the amplitude and shape of $f(\nu)$ does depend on redshift and cosmology in a complicated manner, which depends on the halo definition, and can modify by up to 10 per cent the expected abundance of haloes of a given mass. This can be easily the leading theory systematic error in the cosmological analysis of future cluster catalogues (Artis et al. 2021).

One of the main goals of this paper is to explore the non-universality of the halo mass function. That is, the dependence of the abundance of dark matter haloes on cosmology and/or redshift in addition to that on the linear rms variance of fluctuations, $\sigma(M)$. For this, we will consider cosmologies with identical values for $\sigma(R)$ at $z = 0$, but with very different growth histories. In this way, any signal of non-universality can be attributed to the way in which haloes grow, since the statistics of the initial fluctuation field are identical. This can shed light on the origin of the mass function non-universality and allow for a more accurate modelling. In addition, we will consider simulations with fixed growth history but varying the power spectrum of primordial fluctuations.

Indeed, we will show that by explicitly accounting for the dependence of $f(\nu)$ on the growth rate and power spectrum slope, we are able to predict the halo mass function with a 2–3 per cent accuracy over essentially the whole currently viable cosmological parameter space, including dynamical dark energy. Moreover, this modelling allows to improve the accuracy with which cosmology-rescaling algorithms predict the abundance of haloes.

The outline of this paper is as follows. In Section 2, we describe the cosmological models and the respective N -body simulation we carry out. In Section 3, we measure the non-universality of our simulated halo catalogues and illustrate its physical origin by comparing haloes across simulations. In Section 4, we model the departures from universality as a function of an effective growth rate and power spectrum slope in each cosmological model. In Section 5, we validate these predictions against the halo mass function as measured in a suite of simulations spanning a broad range of cosmological parameters. We further show in Section 6 that our proposed model can be employed to improve the accuracy of cosmology-rescaling techniques. Finally, we conclude and summarize our findings in Section 7.

Table 1. The cosmological parameters that we vary to obtain the nine cosmological models we simulate. We keep the rest of the cosmological parameters fixed assuming flat cosmology and $\Omega_b = 0.046$, $\sigma_8 = 0.82$, $h = 0.677$, $\Omega_\nu = 0.$, $w_0 = 0.0$, $w_a = 0.0$.

	extreme1	central	extreme2
n_s	0.75	0.75	0.75
	0.9611	0.9611	0.9611
	1.25	1.25	1.25
Ω_m	1.	0.307	0.148
Ω_Λ	0.	0.693	0.852

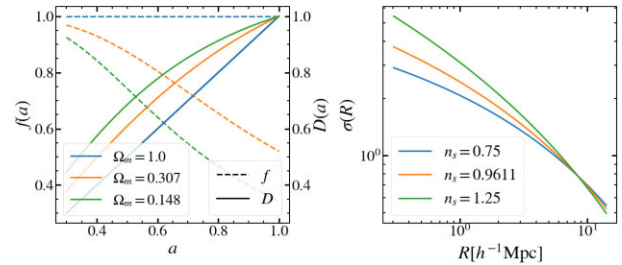


Figure 1. Linear properties of the cosmological models we consider and simulate throughout this paper. Left-hand panel: growth factor, $D(a)$ and growth rate, $f(a)$, as a function of the expansion factor a . Right-hand panel: linear mass variance at $z = 0$ as a function of the Lagrangian radius of haloes of mass M .

2 NUMERICAL SIMULATIONS

In this section, we will describe our set of cosmological simulations and our measurements of the halo mass function. Specifically, in Section 2.1, we describe the cosmological models we consider and in Section 2.2 the numerical setup of the respective simulations. In Section 2.3, we discuss our measurements of the halo mass function, and how we account for numerical and discretization errors.

2.1 Cosmological models

We will consider nine cosmological models given by a combination of three different growth histories and three linear power spectra. In this way, we can explore the effect of the growth history at a fixed linear mass variance, and of the power spectrum shape at a fixed growth history. We note that, in practice, we obtain varying growth histories by defining them with different values of the matter density parameter, Ω_m , and vary the power spectrum shape by considering different values of the primordial spectral index n_s (see Table 1).

In the left-hand panel of Fig. 1, we show the linear growth factor, $D(a)$, and growth rate, $f \equiv \frac{d \log D}{d \log a}$, as a function of expansion factor a of the models we will consider. By construction, at $z = 0$ all models have the same linear amplitude, however, they show very different values for the linear growth rate. At one extreme (green lines), we have a cosmology where structure initially grew very quickly and then stalled, where we expect very little mass accretion today. At the other extreme (blue lines) is a cosmology where structure has been growing at the same pace through the history of the universe, and in particular, we expect it to yield the highest present-day accretion rates on to dark matter haloes.

In the right-hand panel of Fig. 1, we show the three different $\sigma(R)$ at $z = 0$ we consider. The respective power spectra are given by linear predictions for a cosmology consistent with recent observational constraints (cf. Table 1), for three different values of the primordial

Table 2. The main numerical parameters of our simulations. L is the box size; ϵ is the gravitational softening length; and m_p is the mass of each N -body particle.

$L(h^{-1} \text{Mpc})$		200	600	1200	2400
$\epsilon(h^{-1} \text{Mpc})$		0.004	0.012	0.023	0.047
$m_p(h^{-1} M_\odot/1e10)$	extreme1	0.207	5.58	44.67	357.3
	central	0.064	1.71	13.7	109.7
	extreme2	0.031	0.82	6.62	52.9

spectral index, $n_s = \{0.75, 0.96, 1.25\}$. Although these values are clearly inconsistent with current data, they will allow us to clearly identify the role of the shape of fluctuations at a fixed growth history. Specifically, the cosmology with $n_s = 0.75$ displays a very flat power spectrum, thus the density field has more similar fluctuations on all scales. We expect this to yield to similar collapse redshifts among different halo masses. On the other hand, the case with $n_s = 1.25$ features stronger small-scale fluctuations, thus we expect small haloes collapsing at high redshifts and large haloes forming at progressively later time.

2.2 N-body simulations

For each cosmological model described in the previous subsection, we have carried out a suite of cosmological simulations with $N = 1024^3$ particles and four different box sizes, $L = \{200, 600, 1200, 2400\} h^{-1} \text{Mpc}$. This allows us to compute the halo mass function over a broad range of halo masses with a sufficient statistical accuracy at a moderate computational cost. Therefore, in total we have a suite of 36 simulations. The details of the simulations are listed in Table 2.

Each of our simulations is initialized at $z = 49$ using second-order Lagrangian perturbation theory. As recently pointed out by Michaux et al. (2020), this configuration is expected to be accurate at the 2 per cent level for the abundance haloes resolved with more than 100 particles.

We carry out our simulations with an updated version of the L-Gadget3 code (Angulo et al. 2021), employing 48 MPI Tasks. In all cases, we set the Plummer-equivalent softening length to a 2 per cent of the mean interparticle separation. Each of our simulations took approximately 1–3 thousand CPU hours, depending on the mass resolution of the simulation.

2.3 Halo catalogues and discreteness correction

We construct halo catalogues employing a Friends-of-Friends (FoF) algorithm with a linking length parameter $b = 0.2$ at the $z = \{0, 0.5, 1\}$ simulation outputs. Additionally, for each FoF halo, we compute the spherical-overdensity masses $M_\Delta = \frac{4\pi}{3} \Delta r_\Delta^3$, for $\Delta = \{200\rho_c, 200\rho_b, \Delta_{\text{vir}}\}$, where ρ_b is the mean matter density of the universe, and $\Delta_{\text{vir}} \equiv \rho_c \{18\pi^2 - 82[1 - \Omega_m(z)] - 39[1 - \Omega_m(z)]^2\}$ is the virial overdensity expected at each cosmological model. For each mass definition, we compute the halo mass function by considering haloes with more than 32 particles in equally spaced logarithmic bins, $\Delta \log M = 0.155$.

It is known that the FoF algorithm suffers from effects related to particle discreteness, which leads to an overestimation of the mass function (see e.g. Leroy et al. 2021, and references therein). In Warren et al. (2006), an empirical formula was derived to correct for these effects. In agreement with Lukić et al. (2009) and More et al. (2011), we have, however, found that the performance of this correction

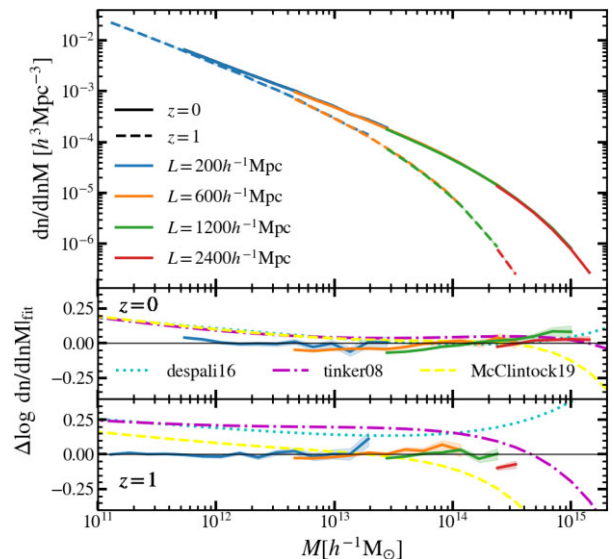


Figure 2. The differential abundance of M_{200b} haloes in one of our cosmological models ($\Omega_m = 0.307$, $n_s = 0.9611$) at $z = 0$ and 1, as estimated in four cosmological simulations of various sizes. The middle and bottom panels display the measurements relative to the expectations of the fitting function with dependence on n_{eff} and α_{eff} developed in this work. The shaded regions correspond to the Poisson uncertainty of the measurements. Moreover, for comparison, dotted and dashed lines display the fitting functions developed in Despali et al. (2015) and Tinker et al. (2008), as well as the emulator presented in McClintock et al. (2019), as indicated by the legend.

varied greatly with cosmology and redshift. In addition, finite numerical precision in the force calculation and time-integration, as well as the effect of softening length, also affect the abundance of haloes detected by FoF (Ludlow, Schaye & Bower 2019). Thus, we have followed a conservative approach and impose a cut of 200 particles per halo without any additional correction. This limit, as shown by Ludlow et al. (2019) is enough to keep all the numerical effects below 5 percent for all mass definitions. Consequently, we will add in quadrature to Poisson errors this 5 per cent to account for possible systematic errors in the measurement of our mass functions.

2.4 Finite volume and output redshift corrections

In order to span a broad mass range, we have combined simulations of many box sizes. For different box sizes, however, the output times can vary slightly since in L-Gadget3 we choose them to coincide with a global time-step which, in turn, can vary from simulation to simulation. In Appendix B, we describe and validate a simple model with which we account for this effect in our measurements.

In addition, the lack of modes larger than the simulated box will induce systematic differences among different box sizes (e.g. Power & Knebe 2006; Lukić et al. 2007; Reed et al. 2007). However, we have checked that for all the boxes these effects are sub-per cent at the relevant masses.

In Fig. 2, we display our measured M_{200b} halo mass function at $z = 0$ and 1 for the cosmological model with $\Omega_m = 0.307$ and $n_s = 0.9611$. Results from simulations of various box sizes (after the corrections described above) are denoted by different line colours, as indicated by the legend.

The top panel displays the differential mass function whereas the middle and bottom panels display the ratio with respect to the predictions of a fitting function we will develop later in this work.

Note we only display bins with more than 400 objects resolved with at least 200 particles. We can see how our suite of various box sizes complement each other to cover a very large range of halo masses, from 5×10^{11} up to $10^{15} h^{-1} M_{\odot}$. The agreement in the overlapping regions is always better than 5 per cent, consistent with our systematic error estimate. Although not shown here, we have checked that this also holds for the other 8 cosmological models.

For comparison, in the bottom panels, we also display the fitting functions of Despali et al. (2015) and Tinker et al. (2008), and the emulator of McClintock et al. (2019). Although some differences among our data and these models are expected due to differences in the group finder mostly in the low-mass end, the comparison readily highlights the impact of non-universality of the mass function. At $z = 0$, our model and that of Despali et al. (2015), Tinker et al. (2008), and McClintock et al. (2019) are in reasonable agreement. However, at $z = 1$, these fits overestimate by more than 10–15 per cent the abundance of haloes in our simulations. The emulator, that includes explicit redshift evolution of the parameters, yields better results than the fits at $z = 1$. In subsequent sections, we will explore this issue in greater detail.

3 THE DEPENDENCE OF THE MASS FUNCTION ON GROWTH HISTORY

In this section, we will compare how the same linear fluctuation turns into collapsed objects of different mass for different cosmologies. We will then explore the dependence of the mass function on both growth rate and the slope of the power spectrum.

3.1 Examples of haloes matched across simulations

The universality of the mass functions assumes that the mass function is completely described by the linear density field. In order to test this assumption, we have run simulations with very different growth histories that share the same linear density field at $z = 0$. In Fig. 3, we show the simulated density field at $z = 0$ for our $L = 200 h^{-1} \text{Mpc}$ simulations with the most dissimilar growth histories for the $n_s = 0.9611$ cosmology. In the top panel, we show a region of $200 h^{-1} \text{Mpc}$ wide, whereas in the middle and bottom panels, we zoom on a massive dark matter halo of normalized mass $M_{200b}/\rho_b \sim 8.5 \times 10^3 h \text{Mpc}^3$. We can see that, although both cases corresponding to identical $z = 0$ linear density peaks, their non-linear counterparts are different. Specifically, in the case, with the highest Ω_m value, and thus, highest current growth rate (in the right-hand panel), haloes are significantly less dense in its center, which is consistent with its expected lower formation redshift and thus lower concentration parameters. Various definitions of halo radii are displayed by white circles in each case. By comparing r_{200c} and r_{vir} radii in the two cosmologies, we see that they identify very different regions of the halo, unlike r_{200b} which is similar in both cases.

To explore this further, we will compare haloes of the same peak height in different simulations. In particular, we have cross-matched halo catalogues among simulations that share the same linear power spectrum at $z = 0$. For this, we associate two haloes based on their position and peak height. From Fig. 3, we expect that the same fluctuation in the linear density field will end up having a different mass depending on its non-linear evolution.

We will characterize each halo by an ‘effective growth rate’ and an effective ‘local power spectrum slope’, which we define, respectively, as

$$\alpha_{\text{eff}}(a) \equiv \left. \frac{d \log(D)}{d \log a} \right|_{a=a_{\text{ev}}}, \quad (3)$$

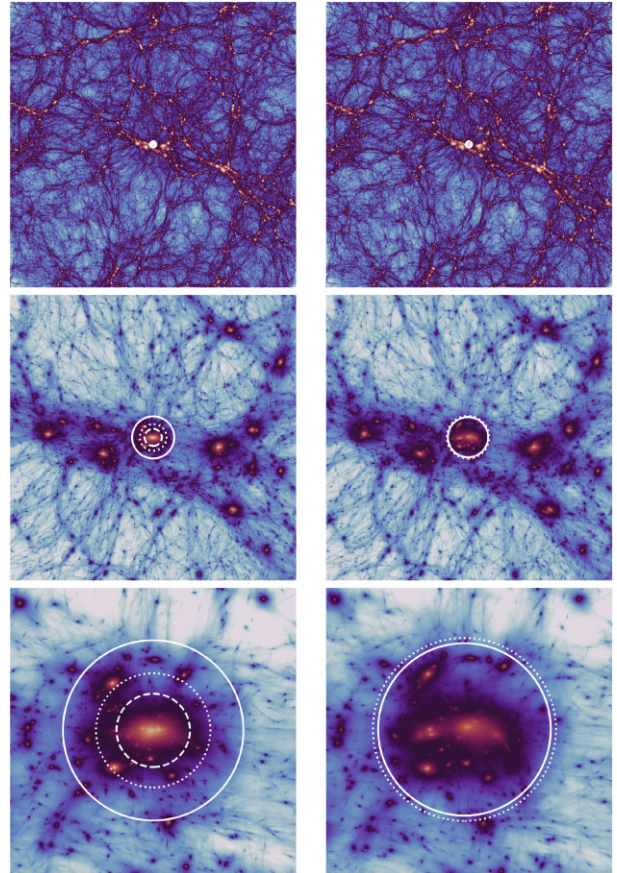


Figure 3. The projected simulated density field normalized by the mean background density at $z = 0$ for two cosmological models that share the same linear density field but differ significantly in their current growth rate. Top panels show the full simulated box, $L = 200 h^{-1} \text{Mpc}$, whereas the middle panels and bottom panel show zooms into regions of 30 and $7 h^{-1} \text{Mpc}$ a side centred in a halo of normalized mass $M_{200b}/\rho_b \sim 8.5 \times 10^3 h \text{Mpc}^3$. In the left-hand column, we plot the cosmological simulation with the lowest matter density $\Omega_m = 0.148$, whereas in the right-hand panel, we display that with the highest matter density, $\Omega_m = 1$. The solid, dashed, and dotted circles show r_{200b} , r_{200c} , and r_{vir} radii of the halo.

where a_{ev} is defined implicitly via $D(a_{\text{ev}}) = \gamma D(a)$ with $\gamma = 4/5$, and

$$n_{\text{eff}} \equiv -3 - 2 \left. \frac{d \log \sigma(R)}{d \log R} \right|_{\kappa R_L(M)}, \quad (4)$$

where $\kappa = 1$, and R_L is the Lagrangian radius of a halo of mass M . Physically, these two parameters will be capturing how quickly haloes have recently grown and the density profile of the collapsing region, which can be considered as a proxy for the full mass accretion and merger history of a given halo.

Note that the effective growth rate is not evaluated at the redshift in which we identify a halo, but it is evaluated in the past, i.e. $\gamma < 1$. By this, we seek to capture not the rate of current mass accretion, but instead the amount of mass that has been accreted recently. We have tried different definitions of α_{eff} and found that this distinction was particularly important for models with dynamical dark energy. We chose the numerical value for γ as that which provided the most accurate and simplest model for the halo mass functions, as we will show in Section 6.

In Fig. 4, we display the spherically averaged mass distribution around cross-matched haloes in 2 bins of the peak height, $\nu \sim 1$

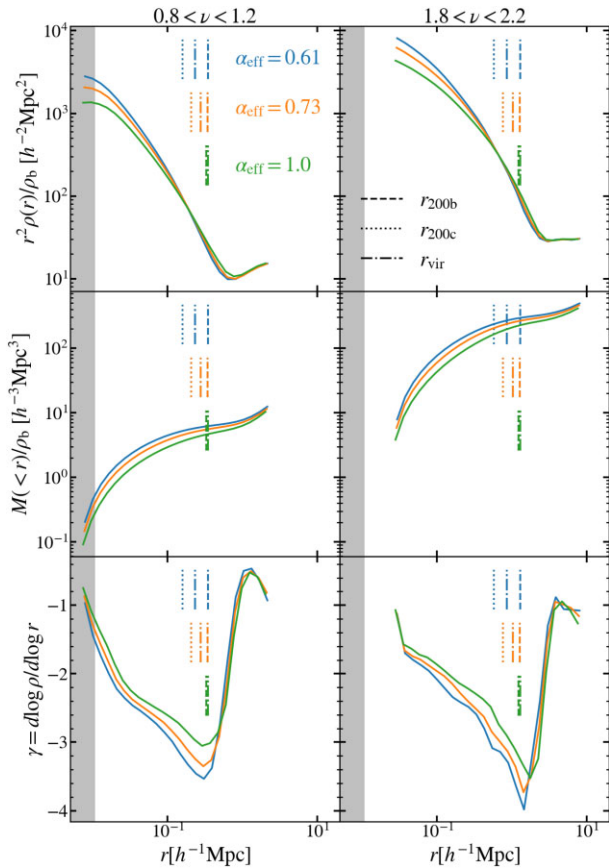


Figure 4. The profiles of the cross-matched haloes with the same linear density field for two ν bins. In the first row, we display the density profiles, in the second row the cumulative mass and in the third row the logarithmic slope of the density profile. The vertical lines indicate the values of r_{200c} , r_{vir} , and r_{200m} radii. The shaded area represents $r < 2.7\epsilon$, where ϵ is the softening length.

and ~ 2 . We display the average density profile, the cumulative mass profile, and the logarithmic slope of the halo density profiles. Vertical lines indicate the radius at which the average enclosed density reaches a value equal to 200 times the background, virial and critical density, as indicated in the legend. Coloured lines indicate three growth histories for the simulations with $n_s = 0.9611$.

We can see that generically the mass profiles differ systematically with α_{eff} , at all values of ν . The higher the growth rate the lower the enclosed mass with respect to the background density at a given physical radius. We emphasize that all these objects share the same shape and amplitude of their linear overdensity field at $z = 0$. Thus, all changes necessarily are caused by the different growth history.

The different growth histories are expected to influence the internal structure of haloes. In particular, lower growth rates are expected to cause lower current accretion rates on to haloes, which implies haloes formed earlier and thus are expected to have higher concentrations. In the first row of panels, we see that this is indeed the case. Inner regions of haloes appear more concentrated. However, the changes are not limited to the concentration, as external parts are also modified increasing their density the higher the current growth rate. In fact, there seems to be an inflection point located at around r_{200c} radius.

Despite the systematic dependence on α_{eff} , the profiles are very similar when expressed in physical units. However, as a consequence

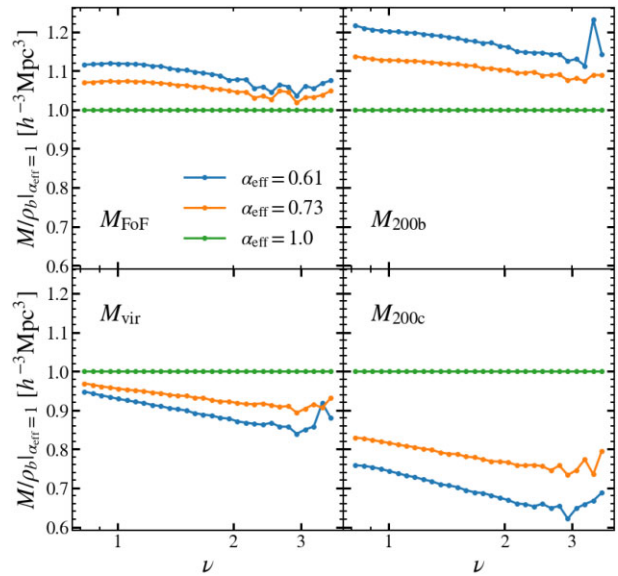


Figure 5. The mass ratio of the cross-matched haloes at $z = 0$ respect to the self-similar cosmology, i.e. $\alpha_{\text{eff}} = 1$. The colours depict the current growth rate value of the given cosmology. In each panel, we display the ratios for M_{FoF} , M_{200b} , M_{vir} , and M_{200c} mass definitions.

of the pseudo-evolution of the halo boundaries (Diemer, More & Kravtsov 2013), when expressed in r_{Δ} units the profiles become very different. The pseudo-evolution of the boundaries is clear in Fig. 4. In the $\alpha_{\text{eff}} = 1$ cosmology, r_{200c} is almost three times larger than in the $\alpha_{\text{eff}} = 0.343$ case, while r_{200b} radii remain roughly constant. Thus, depending on how we define the boundary of our halo, the mass differences will be enhanced or suppressed.

In the lower panels of Fig. 3, this can be appreciated visually. The panels show the most massive cross-matched halo at $z = 0$ in $\alpha_{\text{eff}} = 0.343$ (left-hand panel) and $\alpha_{\text{eff}} = 1$ (right-hand panel) cosmologies. The dashed, dotted, and solid lines represent r_{200c} , r_{vir} , and r_{200b} radii of the halo, respectively. While r_{200b} defines a halo boundary roughly at the same physical location, r_{200c} compares very different regions of the density field. This effect is less important for r_{vir} , which might explain why Despali et al. (2015) found that M_{vir} is the mass definition that leads to the most universal behaviour.

In order to explore this effect more systematically, in Fig. 5, we show how the masses of the cross-matched haloes differ depending on the growth history and the mass definition. We display the ratio of the masses of the cross-matched haloes with respect to the $\alpha_{\text{eff}} = 1$ cosmology as a function of ν . We see that in the cosmology with the lowest current growth rate M_{200c} masses are around 30 percent smaller than in our reference cosmology. However, for the same cosmologies and haloes, M_{200b} masses are around 20 percent more massive.

This effect has two contributions. On the one hand, r_{200c} radii lie in the inner parts where the effect of the growth history on the mass profile is larger. On the other hand, because of the pseudo evolution of r_{200c} , we compare the masses enclosed in different physical radii. As a consequence, even if at a given physical radius the enclosed mass is always larger for haloes in low growth rate cosmologies, when comparing M_{200c} masses it seems that haloes in high growth rate cosmologies are more massive. Note that this is solely because we compare masses enclosed in different physical regions. Thus, the non-universality of M_{200c} mass function is in a big part due to the evolution of the boundary itself.

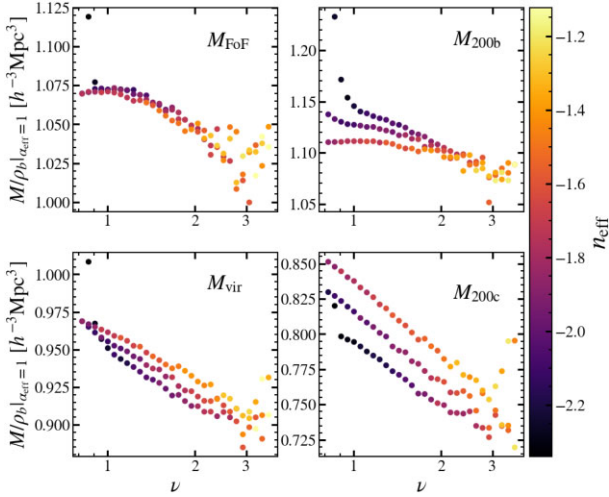


Figure 6. The mass ratio of the cross-matched haloes at $z = 0$ with respect to the cosmological model with self-similar growth, i.e. $\alpha_{\text{eff}} = 1$, and identical linear density field. The colours represent the n_{eff} values of the cross-matched haloes. In each panel we display the ratios for M_{FoF} , M_{200b} , M_{vir} , and M_{200c} mass definitions.

Finally, we want to explore the effect of the local slope of the power spectrum in the cross-matched haloes. For a given power spectrum, redshift and ν , n_{eff} is completely determined. Therefore, in order to see the effect of this variable on the mass of the haloes, we cross-match the cosmologies with $\alpha_{\text{eff}} = 0.52$ and 1 for the three power spectra defined with the three n_s values we have considered in this work. Note that we only cross-match cosmologies with the same linear power spectrum. However, if the local power spectrum slope affects the mass of the haloes, we expect the departures of the masses of $\alpha_{\text{eff}} = 0.52$ from $\alpha_{\text{eff}} = 1$ cosmology to be different in the three linear density fields. In Fig. 6, we show the results following Fig. 5, coloured by the n_{eff} values of the cross-matched haloes. Indeed, we see that for a given ν , the departures of $\alpha_{\text{eff}} = 0.52$ haloes from $\alpha_{\text{eff}} = 1$ haloes are different depending on the n_{eff} value of the halo. Nevertheless, these differences are much smaller than the differences that haloes with different α_{eff} show.

In summary, the whole density profile of the halo is affected by the growth history in a non-trivial way. This effect will be reflected in the mass function in a different fashion depending on how masses are defined. Specifically, we expect the non-universality of the mass function to change with the mass definition.

3.2 The non-universality of the mass function

From the numerical simulations described in the previous section, we have obtained measurements of the halo mass function in nine cosmologies – three growth histories and three different power spectrum slopes – covering a broad range of masses at various redshifts.

In order to compare these measurements and estimate the impact of the non-universality in the mass function, we have computed $\nu f(\nu)$, where ν is $\delta_c/\sigma(M)$. Operationally, we first measure the mass function $n(M)$ and then estimate $\nu f(\nu)$ inverting equation (1).

The critical density for collapse, $\delta_c(z)$, can be estimated as $3/5(1.5\pi)^{2/3}\Omega_m(z)^{0.005}$ (Kitayama & Suto 1996), with an explicit dependence on Ω_m . In this work, we approximate it with the value that corresponds to a universe where there is only matter, $\delta_c = 1.686$. We do this to simplify the redshift and cosmology dependence and make

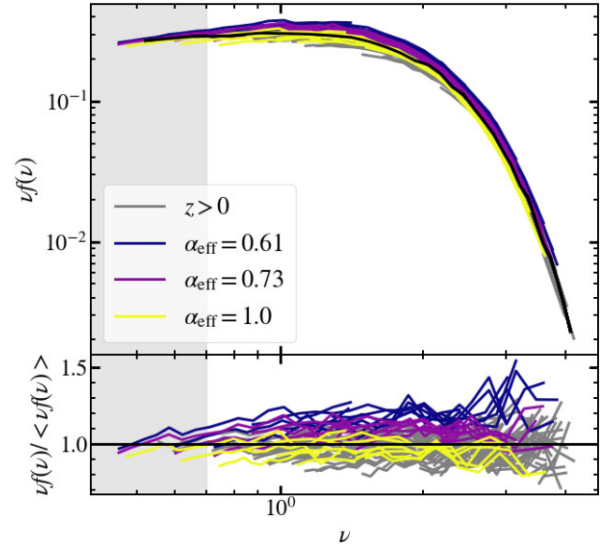


Figure 7. The measured M_{200b} mass functions of the nine cosmological models considered in this work at $z = 0, 0.5$, and 1. The bottom panel shows the ratio relative to the mean value in each ν bin. We show in grey the $z > 0$ mass functions, while we colour the $z = 0$ mass functions according to their α_{eff} value. The shaded area corresponds to measurements with $\nu < 0.7$, which will be excluded when developing a fitting function for $f(\nu)$.

it easier to model. We have checked that the deviations from universal behaviour of the mass function are stronger (up to ± 30 per cent) than the effect of taking into account the redshift evolution of the critical overdensity for collapse, which changes the results around ± 10 per cent (see Appendix A).

In Fig. 7, we display the measurements of $\nu f(\nu)$ from M_{200b} mass function in the cosmologies listed in the Table 1 at $z = 0, 0.5$, and 1. The mass functions with $z > 0$ are displayed as grey lines, while $z = 0$ mass functions are coloured according to their α_{eff} value. The average value in each ν bin is displayed as a black solid line, and it is used as a reference for the ratio displayed in the bottom panel. To avoid possible biases due to differential coverage of our models,¹ we will restrict our subsequent analysis to the range $0.7 < \nu < 5$. For the cosmology most consistent with observational constraint, this implies a mass range of $10^{11} < M/[h^{-1}M_\odot] < 10^{15}$ at $z = 0$.

In this figure, we can clearly see deviations from an universal behaviour. For ν values above unity, haloes of a given peak height in one cosmology can be up to 70 per cent more abundant than in others. By construction, the origin of this non-universal behaviour must be in a combination of the different statistics of the initial Gaussian random fields and the different growth histories. Indeed, we can already see that this is the case for the cosmologies that share the same linear density field at $z = 0$. At a given ν , haloes seem to be more abundant the lower the growth rate value. Recall that, as we saw in the previous section, this is a consequence of the same fluctuation being more massive for low growth rate values.

We now explore how these deviations correlate with the value of the effective growth rate and power spectrum slope at any redshift. In Fig. 8, we display the deviations from the average $\nu f(\nu)$ as a function of n_{eff} and α_{eff} ; that is, $\nu f(\nu)/\langle \nu f(\nu) \rangle$, where the average is computed among all our simulations at fixed ν . Each panel shows

¹At a fixed volume and number of particles, the differences in the power spectrum shape and Ω_m lead to differences in the range of ν -peaks that our simulations are able to resolve.

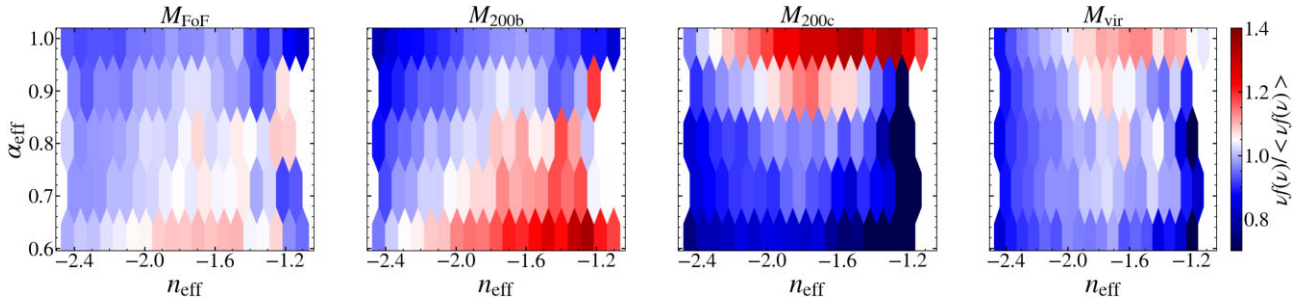


Figure 8. The deviation of the mass function from the average $\nu f(\nu)$ computed among all our simulations at fixed ν , plotted according to the α_{eff} and n_{eff} values. The panels correspond to different mass definitions.

the result for a different mass definition. The results are similar if we use the median instead of the mean.

For all mass definitions, we can see that the non-universality clearly correlates with these properties – despite them being only a proxy of very different merger and assembly histories. In the second panel, we see that for M_{200b} , deviations around the mean can reach ± 20 per cent. Cosmologies that have higher-than-the-mean $\nu/\bar{\nu}$ typically have lower growth rate values, whereas those with higher growth rate values lead to lower abundances. At fixed α_{eff} , deviations from universality are much smaller, about 15 per cent, and they correlate with n_{eff} . Note that here we are plotting measurements of many redshifts, therefore, we expect that the redshift evolution of the mass function could be described through the dependence on these physically motivated variables.

However, the non-universality of the mass function depends on the mass definition. Among those considered in this work, M_{200c} (M_{FoF}) mass functions are the most (least) non-universal with deviations up to ± 30 per cent (± 10 per cent) around the mean. It is interesting to note that, as Despali et al. (2015) found, M_{vir} mass functions are the most universal among the SO mass functions. Furthermore, the dependence on the growth rate is inverted in M_{200c} and M_{vir} cases with respect to M_{200b} case (in agreement with Diemer 2020).

In summary, haloes of a given peak height, ν_{200b} , are more abundant the lower the growth rates and the shallower the power spectrum slope. In other words, a halo that forms early and has grown mostly through minor mergers, will be more massive than another that has recently formed and has experienced a lot of major mergers, even if both have an identical peak height in the linearly extrapolated initial field.

There could be different paths to follow at this point. One could be to find the halo boundary definition that minimizes the non-universality of the mass function. In fact, we have seen that mass definitions based on the critical density induce strong pseudo-evolution in the mass function driven by the change of the boundary of the halo. One quantity that has been argued is more physical is the turnaround radius, which by definition encloses the outermost shell that has collapsed. In the same direction, the first explorations of the splashback mass functions have been done (Diemer 2020). Other alternatives have been recently proposed, which are claimed separate better the linear and non-linear regimes of the density field and are tightly related to the splashback radius (e.g. Fong & Han 2020; Garcia et al. 2020).

However, there is no perfect mass definition, and the suitability of different candidates depends on the science question one wants to address. Any universal mass definition, as we saw earlier, would correspond to very large scales, which although perhaps better suited for describing the mass distribution, might not describe equally well,

and thus it might display less correlation with the properties of collapsed gas and of the galaxies hosted by the halo. In addition, many of the proposed halo definitions are ambiguous to implement numerically.

Another option would be to develop a model for the changes of the full density profile as a function of the mass accretion history. For instance, in an analogous manner to the models developed for the relationship between the concentration and the expected mass accretion history in Extended Press Schechter (Ludlow et al. 2016, 2019), it is perhaps possible to develop a model for the outer regions of a halo, which would then predict the changes in halo mass at any radius.

The option we will follow here is to adopt a standard halo definition but calibrate the predictions for the halo abundance to be a function of the peak height but also of the properties of the cosmological model. We will show that with a simple parameterization in terms of α_{eff} and n_{eff} , we can accurately describe the halo mass function for a large region in cosmological parameters space.

4 MODELLING THE DEPENDENCE ON GROWTH FUNCTION AND POWER SPECTRUM SLOPE

In the previous sections, we showed how the halo mass function varies systematically with growth rate and slope of the power spectrum. In this section, we will model this dependence explicitly.

We will focus on the M_{200b} mass function, because as it has been discussed in the previous section, it is the most physically motivated choice and presents the least pseudo-evolution among the overdensity mass definitions. FoF mass function could also be a good candidate, but the fact that it has no clear observational counterpart and that the masses are very subject to numerical effects make it a less interesting candidate. However, in Appendix C, we show that our approach is valid to model the mass function of any of the other mass definitions considered in this work.

We have employed the following functional form $f(\nu, n_{\text{eff}}, \alpha_{\text{eff}})$ to model each of our measurements

$$\nu f(\nu, n_{\text{eff}}, \alpha_{\text{eff}}) = \nu f_1(\nu) f_2(n_{\text{eff}}) f_3(\alpha_{\text{eff}}), \quad (5)$$

$$f_1(\nu) = 2A_{\text{mp}} (1 + (a\nu^2)^{-p}) \sqrt{\frac{a\nu^2}{2\pi}} e^{-0.5a\nu^2}, \quad (6)$$

$$f_2(n_{\text{eff}}) = n_0 n_{\text{eff}}^2 + n_1 n_{\text{eff}} + n_2, \quad (7)$$

$$f_3(\alpha_{\text{eff}}) = a_0 \alpha_{\text{eff}} + a_1, \quad (8)$$

where $\{a, p, A_{\text{mp}}, n_0, n_1, n_2, a_0, a_1\}$ are the free parameters of the model, where we have used the same functional form for $f(\nu)$

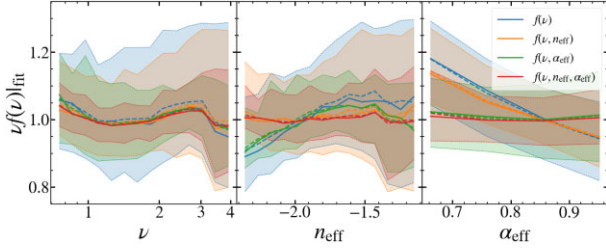


Figure 9. Deviations between $\nu f(\nu)$ measured in our N -body simulations and the predictions of the fitting functions developed in this work. Left-, middle-, and right-hand panels display these deviations as a function of the peak height, ν ; the effective power spectrum slope, n_{eff} ; and the effective growth rate, α_{eff} , respectively. In each panel, shaded regions indicate the region that contains 95 per cent of our simulated results when employing a fitting function calibrated *only* as a function of ν (blue) or additionally including dependence with respect to n_{eff} (green), α_{eff} (orange), or both of them (red). Solid lines indicate the median residual while dashed lines represent the mean.

as Despali et al. (2015). The parametrizations of the n_{eff} and α_{eff} dependencies were inspired by the shape of the deviations from the universal behaviour (blue lines in Fig. 9). We tried higher order polynomials, but the results did not improve noticeably. Notice that the contributions of the variables are separable. Thus, in principle one could calibrate $f(\nu)$ separately, or reuse previously ran simulations.

In each case, we find the best-fitting parameters by minimizing the χ^2 of the quantity $\nu f(\nu)$. We assume a Gaussian Likelihood with a diagonal covariance given by the Poisson error in each bin plus a constant 5 per cent that accounts for systematic errors, as discussed in Section 2. We impose a limit of 200 particles per halo and 400 haloes per mass bin. The minimization is done with the `optimize.minimize` package of `scipy`, imposing bounds on the possible values that the parameters may take. Other than our main model (equation 5), we have found the best-fitting parameters for the functional forms that depend only on ν (equation 6), ν , and n_{eff} (equation 6 \times 7) and ν and α_{eff} (equation 6 \times 8). We list all the best-fitting parameters and the reduced χ^2 values in Table 3. As it can be seen from the reduced χ^2 values, the quality of the fit improves when we add α_{eff} and n_{eff} dependencies. In agreement with what we found in the previous section, α_{eff} dependence seems to be more important than n_{eff} dependence. All in all, reduced χ^2 values vary from 3.26 (the universal fit) to 0.51 (main model), indicating a very good fit.

In order to study the internal degeneracies of the parameters, we check their stability. First, we see that the best-fitting parameters of the universal part are stable and do not change when we add other variables. This is especially true for the amplitude (A_{mp}) and the parameter that controls the exponential suppression of haloes (a). However, it seems that the n_{eff} and α_{eff} parametrizations are somewhat degenerated. Even if the overall sign does not change, the best-fitting parameters vary; mainly the zero-order parameter in n_{eff} (n_2) and the α_{eff} parameters (a_0 and a_1).

We now assess how well this model is able to describe our calibrating data. In Fig. 9, we display the ratio of measured $\nu f(\nu)$, in all our simulations at all three redshifts, to their corresponding predictions of equation (5) (red). In the left-hand, middle, and right-hand panels, we display the residuals as a function of ν , n_{eff} , and α_{eff} , respectively. In all cases, solid and dashed lines display the median and the mean, whereas the shaded areas denote the regions enclosing 95 per cent of the measurements. Thus, this plot quantifies the overall accuracy of each model in describing the mass function diversity we measured.

We can see that indeed, for the full model, $f(\nu, \alpha_{\text{eff}}, n_{\text{eff}})$, the residuals are smaller than ± 10 per cent over the whole range of values explored, with no noticeable remaining dependence with either parameter. For comparison, we display also residuals with respect to a version of equation (6) where we have measured their parameters to our whole data set but only adopting dependence with respect to ν (blue). As expected, in this case, the residuals are significantly larger, reaching variations of ± 20 per cent.

Although the lack of residual dependence with α_{eff} and n_{eff} is achieved by construction, it is in principle not guaranteed that the amplitude of these residuals decrease significantly. For instance, the mass function could have shown dependence on many more details of the assembly history of haloes and the statistics of peaks than simply on the effective growth rate and power spectrum slope. It is, therefore, remarkable that the residuals in the mass function are all contained within a region of ± 10 per cent.

In the next section, we will explore whether our approach is actually able to describe accurately the mass function in multiple cosmologies currently allowed by observational data.

5 VALIDATION: HALO ABUNDANCES AS A FUNCTION OF COSMOLOGY

To assess the accuracy of our description for the halo mass function, we will compare its predictions against a suite of simulations with 30 different cosmologies. Each of our simulations evolved 1536^3 particles inside a box of approximately $L = 512h^{-1}\text{Mpc}$. The initial conditions were created using second-order Lagrangian Perturbation theory at $z_{\text{start}} = 49$ and fixing the amplitude of Fourier modes (Angulo & Pontzen 2016). The cosmologies were chosen so that they cover a region of approximately 10σ around Planck's best-fitting values. Specifically, they cover the following parameters ranges:

$$\begin{aligned}
 \sigma_8 &\in [0.73, 0.86], \\
 \Omega_m &\in [0.23, 0.4], \\
 \Omega_b &\in [0.04, 0.06], \\
 n_s &\in [0.92, 0.99], \\
 h [100 \text{ km s}^{-1} \text{Mpc}^{-1}] &\in [0.65, 0.8], \\
 M_\nu [\text{eV}] &\in [0.0, 0.4], \\
 w_0 &\in [-1.3, -0.7], \\
 w_a &\in [-0.3, 0.3].
 \end{aligned} \tag{9}$$

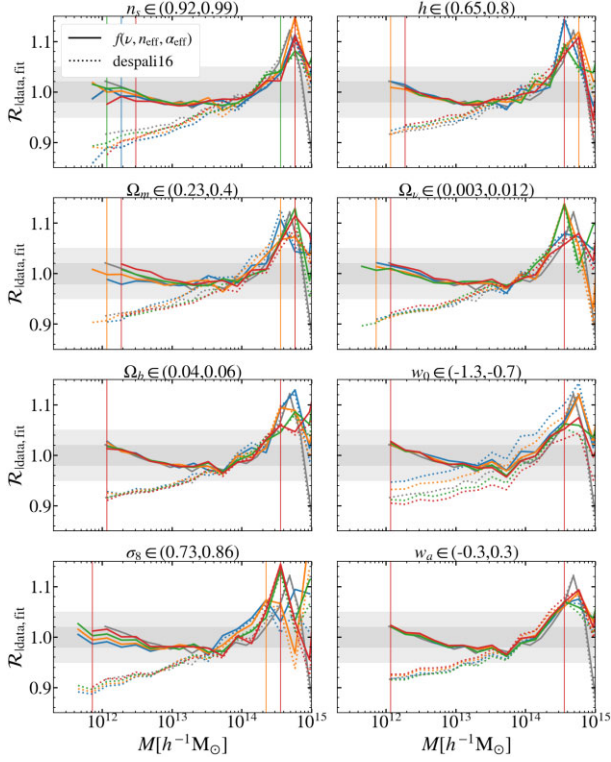
Note these simulations not only cover parameters of the minimal Lambda cold dark matter (ΛCDM) model, but also neutrino masses, M_ν , using the linear response approach of Ali-Haïmoud & Bird (2013); and dynamical dark energy with an equation of state $w(z) = w_0 + (1+z)w_a$. The cosmology of each simulation is obtained by changing one cosmological parameter of a fiducial cosmology while keeping the rest fixed. The fiducial cosmology assumes flat geometry, massless neutrinos ($M_\nu = 0$), a dark energy equation of state with $w_0 = -1$ and $w_a = 0$, an amplitude of matter fluctuations $\sigma_8 = 0.9$, cold dark matter density $\Omega_{\text{cdm}} = 0.265$, baryon density $\Omega_b = 0.05$, and normalized Hubble constant $h = 0.6$.

In Figs 10 and 11, the solid lines represent the measured mass functions of the 30 simulations relative to the predictions of the main model developed in this work (equation 5). We show the limits of the bins with at least 400 haloes with resolved with more than 200 particles as vertical lines.

In each row, we show the mass functions of the cosmologies where we vary one cosmological parameter keeping the rest fixed. In Fig. 10,

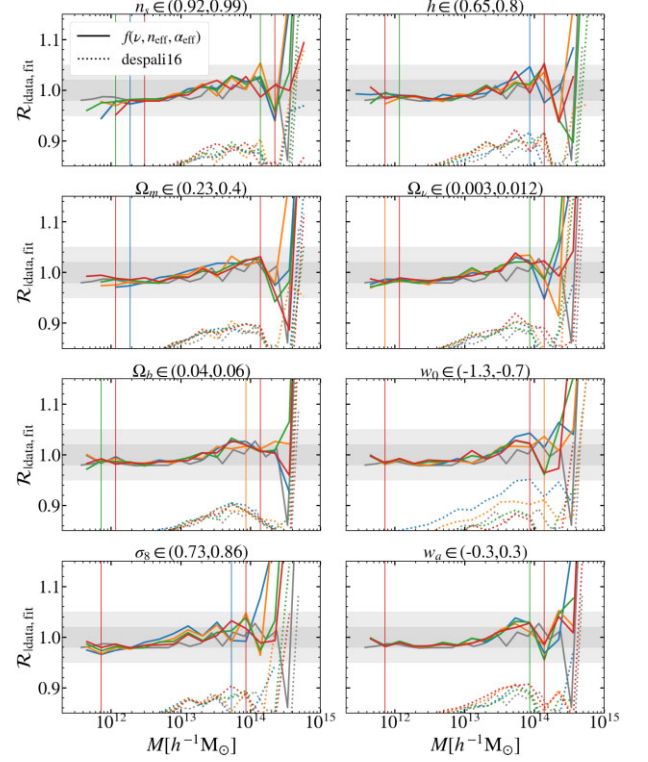
Table 3. A table listing the best-fitting parameters of our M_{200b} -fitting functions and the reduced χ^2 values of the fits.

	a	p	A_{mp}	n_0	n_1	n_2	a_0	a_1	χ^2/ν
$f_1(\nu)$	0.769	0.0722	0.3173	–	–	–	–	–	3.26
$f_1(\nu)f_2(n_{\text{eff}})$	0.7741	0.1746	0.3038	−0.1912	−0.4211	0.9859	–	–	1.98
$f_1(\nu)f_3(\alpha_{\text{eff}})$	0.772	0.0308	0.3069	–	–	–	−0.6255	1.5654	1.22
$f(\nu, n_{\text{eff}}, \alpha_{\text{eff}})$	0.7691	0.1309	0.3092	−0.1178	−0.3389	0.3022	−1.0785	2.97	0.51


Figure 10. Comparison between M_{200b} halo mass functions in multiple cosmologies as measured in N -body simulations relative to the fit developed in this work (solid lines) and the model developed in Despali et al. (2015) (dotted lines), at $z = 0$. We display $\mathcal{R}_{\text{data,fit}} = \frac{dn}{d \ln M} \left(\frac{\text{data}}{\text{fit}} \right)$. The vertical lines display the limits of the bins with at least 400 haloes resolved with more than 200 particles. Each row, from the top to bottom, display variations in n_s , Ω_m , Ω_b , and σ_8 for the first column and h , Ω_ν , w_0 , and w_a for the second column. The grey lines display the result for the fiducial cosmology. The shaded areas denote regions of ± 5 and ± 2 percent.

we display the results at $z = 0$, and in Fig. 11 the results at $z = 1$. For comparison, we also show the residuals respect the model developed in Despali et al. (2015) as dotted lines, which assumes universality of the mass function. We recall that the functional dependence on $f(\nu)$ is the same in both models, while in our model we have added extra dependences on n_{eff} and α_{eff} in order to capture the effect of growth history on the mass function. We have decided not to display the non-universal prediction of McClintock et al. (2019) because our parameter space is larger than theirs, and therefore many of the mass functions would lie outside the tested regime. Moreover, they do not include massive neutrinos and dynamical dark energy.

At $z = 0$, our model describes the low-mass end of the mass function at an accuracy of 3 percent, while Despali et al. (2015) predict that haloes are 10 percent more abundant. This may be a consequence of using different group finders, SO and FoF, respec-


Figure 11. Same as Fig. 10 at $z = 1$.

tively. For haloes with masses above $M > 10^{14} h^{-1} M_\odot$, there seems to be an underprediction of our fitting function. To investigate this, we have compared our predictions against the simulations of Angulo et al. (2021), which feature the same mass resolution as our test suite but on a volume 27 times larger. Although not shown here, in such case we find an agreement to better than 5 percent up to $10^{15} h^{-1} M_\odot$. Combined with the good agreement of our predictions with those of Despali et al. (2015), we speculate that there is a systematic overprediction of the abundance of haloes in our test sims for $M > 10^{14} h^{-1} M_\odot$, which could be caused by finite-volume effects.

At $z = 1$, the redshift evolution of the mass function is evident. Even if at $z = 0$, (Despali et al. 2015) is a good description to the mass function, at $z = 1$ it overpredicts the abundances for more than 10 percent. Our model captures this and yields results that are accurate within 5 percent at all masses considered.

Compared to the redshift evolution, the cosmology dependence of the mass function seems to be weak. However, the mass functions of w_0 cosmologies present strong deviations from universality. The scatter of the ratio with respect to Despali et al. (2015) is of ~ 5 percent among cosmologies with different w_0 values at both redshifts. After taking into account the dependences on α_{eff} and n_{eff} , this scatter vanishes. We emphasize that we have only used Λ CDM

cosmologies to calibrate the fit, and so α_{eff} and n_{eff} are physically meaningful proxies of the non-universality of the mass function.

It is interesting to notice that the largest part of the improvement is obtained when adding α_{eff} to the universal description. This is expected, because as discussed in Section 3, the deviations from universality correlate much stronger with α_{eff} than with n_{eff} .

6 APPLICATION: IMPROVING THE ACCURACY OF COSMOLOGY-RESCALING METHODS

To approach an optimal exploitation of current and future observations of the abundance of dark matter haloes and the clustering of galaxies, very accurate theoretical predictions for these quantities are required. Although fitting functions and calibrated recipes are indeed extremely valuable, they fall short in providing correlations among different observables or the full three-dimensional distribution of clusters of galaxies. One option to obtain those predictions is to employ cosmological N -body simulations together with cosmology-rescaling algorithms.

The basic idea of cosmology rescaling is to employ a few simulations carried out adopting specific cosmological parameters, and then manipulate their outputs so that represent non-linear structure in any other set of cosmologies. These algorithms have been extensively discussed and tested in Angulo & White (2010), Angulo & Hilbert (2015), Ruiz et al. (2011), Mead & Peacock (2014b), Mead & Peacock (2014a), Renneby, Hilbert & Angulo (2018). In particular, Zennaro et al. (2019) showed these are applicable to cases of massive neutrinos, and Contreras et al. (2020) showed that the clustering of dark matter and dark matter haloes and subhaloes can be obtained to better than 3 per cent accuracy from large to very small scales ($0.01 < k/h \text{ Mpc}^{-1} < 5$). This technique has been recently employed by Angulo et al. (2021) to predict the non-linear power spectrum as a function of cosmology, by Aricò et al. (2019), Aricò et al. (2020) to model the effect of baryonic physics and predict the suppression of the power spectrum due to baryons, and by Zennaro et al. (2021) to model the clustering of biased tracers.

In Fig. 12, we check the performance of cosmology rescaling in predicting the halo mass functions. Specifically, we compare measurements in the 30 simulations described in the previous section to the halo mass function after rescaling one simulation. We refer the reader to Contreras et al. (2020) for details on how the cosmologies of these simulations were chosen.

In the original cosmology rescaling, the simulation volume and the particle mass are rescaled by a single factor, found by minimizing the difference in the linear mass variance in the target and rescaled cosmologies. In this operation, the number of particles in each halo is left invariant. Using this recipe, the scaling algorithm sets the same linear density field in the rescaled and target simulations, which is equivalent to assuming the universality of the mass function. However, in this work, we have shown that the mass function depends not only on the linear density field but also on the entire growth history. In fact, we can see that the scaling of the mass function fails in the dotted lines of Fig. 12, where we compare the mass functions from the rescaled simulations with the target ones. By assuming universality of the mass function, the rescaled M_{200b} mass functions differ from the target mass functions up to 10 per cent in some cosmologies at $z = 0$.

Our model for the dependence of the halo mass function on growth history gives us the possibility to construct an additional correction for cosmology rescaling by taking into account the different growth histories the target and rescaled cosmologies have gone through.

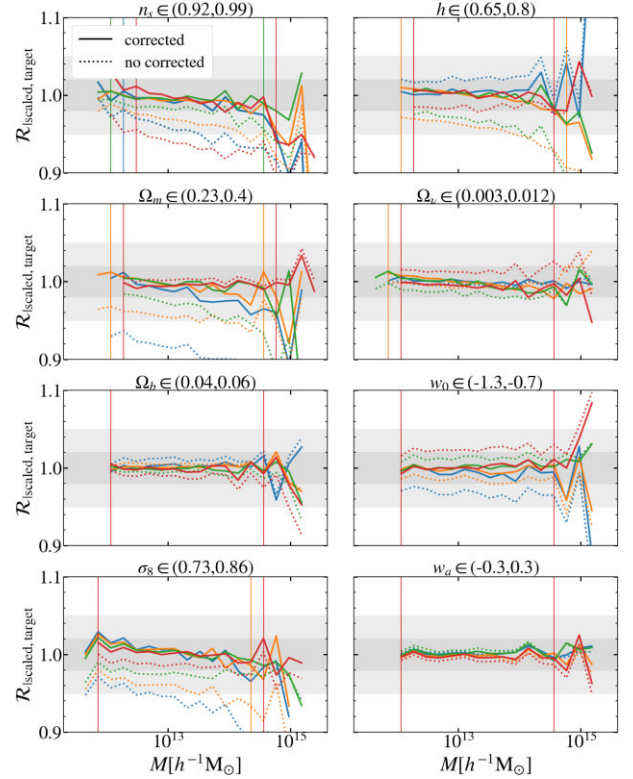


Figure 12. Comparison between M_{200b} halo mass functions in multiple cosmologies as measured in N -body simulations relative to that in cosmology-rescaled simulations at $z = 0$. Specifically, we display $\mathcal{R}_{\text{scaled,target}} = \frac{dn}{d \ln M} \left(\frac{\text{scaled}}{\text{target}} \right)$. The vertical lines display the limits of the bins with at least 400 haloes resolved with more than 200 particles. Each row, from top to bottom, display variations in n_s , Ω_m , Ω_b , and σ_8 for the first column and h , Ω_b , w_0 , and w_a for the second column. In each panel, we show results before (dotted lines) and after (solid lines) applying our additional correction accounting for dependence on growth history, as indicated by the legend (see the text for details). The shaded regions denote regions of ± 5 and ± 2 per cent.

Specifically, we adjust the halo masses depending on the n_{eff} and α_{eff} values of the rescaled and target cosmologies. The procedure is the following: First, we compute the rescaled and target mass functions with our model. In the target cosmology case, the prediction is straightforward. In the rescaled original cosmology case, we compute the expected mass function of the original cosmology once we have applied the corresponding mass and length scalings, i.e., once we have set the linear density field equal to the target cosmology's linear density field. Next, we use the fact that the difference between target and rescaled mass functions is given by a change in mass of the haloes, rather than a change in the abundance of haloes of a given mass (as we have seen in Section 3.1). We find this difference by mapping the rescaled halo masses to the target halo masses where the abundances are the same. Therefore, for a given pair of original-target cosmologies, we can predict a halo-by-halo mass correction to the rescaled haloes that captures the effect of the non-universality of the halo mass function.

We show the results of the rescaling algorithm after applying this correction as solid lines in Fig. 12. We can see that in all cosmologies, the accuracy of the predictions improves in a clear manner. At $z = 0$, the differences are in most of the cases smaller than 2 per cent. Note that our model, calibrated on simulations where we only vary Ω_m and

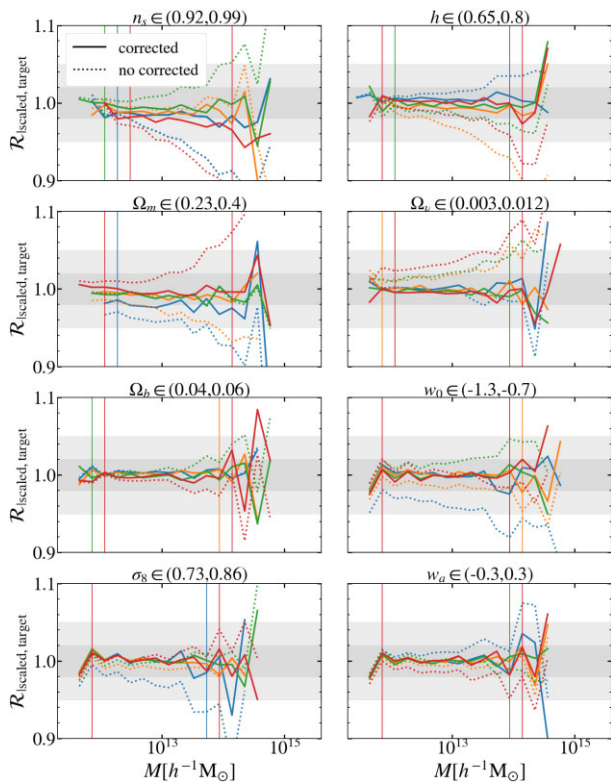


Figure 13. Same as Fig. 12 but at $z = 1$.

n_s , is able to capture the non-universality of general cosmologies, even in beyond Λ CDM cosmologies with massive neutrinos and dynamical dark energy included. As seen in Fig. 13, at $z = 1$ the accuracy is as good as for $z = 0$, reaching ± 1 – 2 per cent over the full range of masses where we can measure the mass function accurately.

7 SUMMARY AND CONCLUSIONS

In this paper, we have studied the non-universality of the halo mass function. We have run simulations with very extreme cosmologies to maximize the deviations from universal behaviour and we have shown that the halo masses are affected by the entire growth history. As a consequence, given the same linear density field in two different cosmologies, the halo mass functions are different.

In order to shed light in the origin of the non-universality of the mass functions, we have cross-matched haloes of different cosmologies that share the same linear density field and we have compared their density profiles. Generally, we have observed that all the density profiles up to very large radii are affected by the growth history of the haloes. Furthermore, the physical boundaries of haloes selected with density criteria are subject to pseudo evolution, and correspond to different physical radii for different cosmologies. This effect is more pronounced for overdensities defined with respect to the critical density of the universe. Therefore, different mass definitions yield mass functions with different dependences on redshift and cosmology.

We have modelled the non-universality of the mass function adding two additional parameters other than the peak-height ν : the effective growth rate, α_{eff} , and the local slope of the power spectrum, n_{eff} . Using a total of eight free parameters, our model captures the non-universality and can lower the scatter on the halo mass functions

in all the cosmologies considered from ± 20 per cent to less than ± 10 per cent up to $z = 1$. In the literature, the redshift evolution of the mass function is typically parametrized explicitly within a fiducial cosmology (see e.g. Tinker et al. 2008; McClintock et al. 2019). On the contrary, here we have modelled simultaneously the cosmology and redshift non-universality of the mass function by using physically motivated parameters.

We have tested our model on an independent set of simulations of 30 different cosmologies, including massive neutrinos and dynamical dark energy. By considering the α_{eff} and n_{eff} dependences, we have been able to reproduce the halo mass functions within a 5 per cent accuracy in all the cosmologies up to $M \sim 5 \times 10^{14} h^{-1} M_{\odot}$ until $z = 1$. We emphasize that the simulations that we have used to calibrate the models have been run with Λ CDM cosmologies. Thus, it is not a trivial result that our model is able to describe the halo mass functions within, for instance, cosmologies that include massive neutrinos or dynamical dark energy.

As an application of our model, we have applied it together with the cosmology rescaling method presented in Angulo & White (2010). We have found that the accuracy in the scaling of the halo mass function improves from 10 to 2 per cent in all cosmologies including dark energy and massive neutrinos, mostly because of the dependency on the growth rate.

There are many paths that we would like to explore in future works. It is well known that baryonic processes alter in non-trivial way the halo mass function. In particular, astrophysical feedback ejects a large amount of gas outside the haloes boundaries, and therefore haloes become less massive, even by when including a baryonic modelling (see Debackere, Schaye & Hoekstra 2020; e.g. Castro et al. 2021). We plan to extend our formalism to include the effect of baryons on the halo mass function, by using the so-called baryonification technique (Schneider & Teyssier 2015; Aricò et al. 2019). By combining it with cosmological-rescaling algorithms, we will construct an emulator of the halo mass functions, as a function of cosmological and astrophysical parameters.

In the near future, more precise and accurate predictions of the halo mass function will be necessary in order to fully exploit the data of the future surveys. As an example, Artis et al. (2021) estimated that, only considering the precision of the parameters of the fitting functions in the analysis (i.e. assuming universality of the mass function), an improvement from 30 to 70 per cent is required. This framework provides us with a very accurate fit of the halo mass function, which can be eventually exploited to directly compare against observed clusters count, from optical, X-ray or Sunyaev–Zel’dovich surveys. Thus, we anticipate that this model will be of great value in constraining the cosmological parameters of the Universe.

ACKNOWLEDGEMENTS

LO acknowledges the Summer Internship Program of the Donostia International Physics Center. The authors acknowledge the support of the ERC-StG number 716151 (BACCO). SC acknowledges the support of the ‘Juan de la Cierva Formación’ fellowship (FJCI-2017-33816). The authors acknowledge computing resources at MareNostrum-IV and the technical support provided by Barcelona Supercomputing Center (RES-AECT-2019-2-0012, RES-AECT-2020-3-0014).

DATA AVAILABILITY

The data underlying this article will be shared on reasonable request to the corresponding author.

REFERENCES

- Abazajian K. et al., 2019, preprint (arXiv:1907.04473)
- Ade P. et al., 2019, *J. Cosmol. Astropart. Phys.*, 2019, 056
- Ali-Haïmoud Y., Bird S., 2013, *MNRAS*, 428, 3375
- Angulo R. E., Hilbert S., 2015, *MNRAS*, 448, 364
- Angulo R. E., Pontzen A., 2016, *MNRAS*, 462, L1
- Angulo R. E., White S. D. M., 2010, *MNRAS*, 405, 143
- Angulo R. E., Springel V., White S. D. M., Jenkins A., Baugh C. M., Frenk C. S., 2012, *MNRAS*, 426, 2046
- Angulo R. E., Zennaro M., Contreras S., Aricò G., Pellejero-Ibañez M., Stücker J., 2021, *MNRAS*, 507, 5869
- Aricò G., Angulo R. E., Hernández-Monteagudo C., Contreras S., Zennaro M., Pellejero-Ibañez M., Rosas-Guevara Y., 2019, *MNRAS*, 495, 4800
- Aricò G., Angulo R. E., Contreras S., Ondaro-Mallea L., Pellejero-Ibañez M., Zennaro M., 2020, *MNRAS*, 506, 4070
- Artis E., Melin J.-B., Bartlett J. G., Murray C., 2021, *A&A*, 649, 18
- Bhattacharya S., Heitmann K., White M., Lukić Z., Wagner C., Habib S., 2011, *ApJ*, 732, 122
- Bocquet S., Saro A., Dolag K., Mohr J. J., 2016, *MNRAS*, 456, 2361
- Bocquet S., Heitmann K., Habib S., Lawrence E., Uram T., Frontiere N., Pope A., Finkel H., 2020, *ApJ*, 901, 5
- Bonoli S. et al., 2020, *A&A*, 653, 37
- Castro T., Borgani S., Dolag K., Marra V., Quartin M., Saro A., Sefusatti E., 2021, *MNRAS*, 500, 2316
- Contreras S., Zennaro R. E. A. M., Aricò G., Pellejero-Ibañez M., 2020, *MNRAS*, 499, 4905
- Courtin J., Rasera Y., Alimi J.-M., Corasaniti P.-S., Boucher V., Füzfa A., 2011, *MNRAS*, 410, 1991
- Crocce M., Fosalba P., Castander F. J., Gaztañaga E., 2010, *MNRAS*, 403, 1353
- Debackere S. N. B., Schaye J., Hoekstra H., 2020, *MNRAS*, 492, 2285
- Despali G., Giocoli C., Angulo R. E., Tormen G., Sheth R. K., Baso G., Moscardini L., 2015, *MNRAS*, 456, 2486
- Diemer B., 2020, *ApJ*, 903, 87
- Diemer B., More S., Kravtsov A. V., 2013, *ApJ*, 766, 25
- Fong M., Han J., 2020, *MNRAS*, 503, 4250
- García R., Rozo E., Becker M. R., More S., 2020, *MNRAS*, 505, 1195
- Hofmann F. et al., 2017, *A&A*, 606, A118
- Ivezić Ž. et al., 2019, *ApJ*, 873, 111
- Jenkins A., Frenk C. S., White S. D. M., Colberg J. M., Cole S., Evrard A. E., Couchman H. M. P., Yoshida N., 2001, *MNRAS*, 321, 372
- Kitayama T., Suto Y., 1996, *ApJ*, 469, 480
- Leroy M., Garrison L., Eisenstein D., Joyce M., Maleubre S., 2021, *MNRAS*, 501, 5064
- Ludlow A. D., Bose S., Angulo R. E., Wang L., Hellwing W. A., Navarro J. F., Cole S., Frenk C. S., 2016, *MNRAS*, 460, 1214
- Ludlow A. D., Schaye J., Bower R., 2019, *MNRAS*, 488, 3663
- Lukić Z., Heitmann K., Habib S., Bashinsky S., Ricker P. M., 2007, *ApJ*, 671, 1160
- Lukić Z., Reed D., Habib S., Heitmann K., 2009, *ApJ*, 692, 217
- McClintock T. et al., 2019, *ApJ*, 872, 53
- Mead A. J., Peacock J. A., 2014a, *MNRAS*, 440, 1233
- Mead A. J., Peacock J. A., 2014b, *MNRAS*, 445, 3453
- Michaux M., Hahn O., Rampf C., Angulo R. E., 2020, *MNRAS*, 500, 663
- Mo H., van den Bosch F., White S., 2010, *Galaxy Formation and Evolution*. Cambridge Univ. Press, Cambridge
- More S., Kravtsov A. V., Dalal N., Gottlöber S., 2011, *ApJ*, 195, 4
- Power C., Knebe A., 2006, *MNRAS*, 370, 691
- Press W. H., Schechter P., 1974, *ApJ*, 187, 425 (PS)
- Reed D., Gardner J., Quinn T., Stadel J., Fardal M., Lake G., Governato F., 2003, *MNRAS*, 346, 565
- Reed D. S., Bower R., Frenk C. S., Jenkins A., Theuns T., 2007, *MNRAS*, 374, 2
- Renneby M., Hilbert S., Angulo R. E., 2018, *MNRAS*, 479, 1100
- Ruiz A. N., Padilla N. D., Domínguez M. J., Cora S. A., 2011, *MNRAS*, 418, 2422
- Sartoris B. et al., 2016, *MNRAS*, 459, 1764
- Schneider A., Teysier R., 2015, *J. Cosmol. Astropart. Phys.*, 2015, 049
- Seppi R. et al., 2020, *A&A*, 652, 25
- Sheth R. K., Tormen G., 1999, *MNRAS*, 308, 119
- Sheth R. K., Tormen G., 2002, *MNRAS*, 329, 61
- Tinker J., Kravtsov A. V., Klypin A., Abazajian K., Warren M., Yepes G., Gottlöber S., Holz D. E., 2008, *ApJ*, 688, 709
- Warren M. S., Abazajian K., Holz D. E., Teodoro L., 2006, *ApJ*, 646, 881
- Watson W. A., Iliev I. T., D'Aloisio A., Knebe A., Shapiro P. R., Yepes G., 2013, *MNRAS*, 433, 1230
- Weinberg D. H., Mortonson M. J., Eisenstein D. J., Hirata C., Riess A. G., Rozo E., 2013, *Phys. Rep.*, 530, 87
- Zennaro M., Angulo R. E., Aricò G., Contreras S., Pellejero-Ibañez M., 2019, *MNRAS*, 489, 5938
- Zennaro M., Angulo R. E., Pellejero-Ibañez M., Stücker J., Contreras S., Aricò G., 2021, preprint (arXiv:2101.12187)

APPENDIX A: COSMOLOGY AND REDSHIFT DEPENDENT CRITICAL DENSITY

In this appendix, we show the effect of taking into account the redshift dependence of the critical density for collapse on the non-universality of the mass function. Specifically, we compute the relative difference of the deviations in each ν bin between the mass functions with $\delta_c(z)$ and $\delta_c = 1.686$.

In Figs A1 and A2, we show these relative differences for two different approaches of computing $\delta_c(z)$. We see that, for most of the cases they do not exceed the ± 10 per cent, while the deviations around the mean are much stronger, as we can see in Fig. 8.

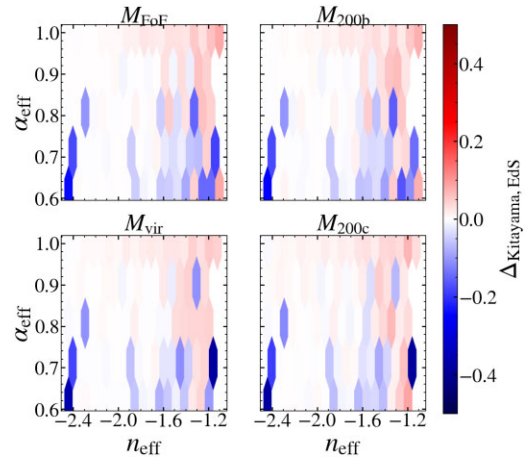


Figure A1. The difference of the deviations of the mass function respect to the mean computed in each ν bin between the mass functions obtained with the critical density for collapse presented in (Kitayama & Suto 1996) and with the critical density corresponding to a universe with only matter. $\Delta_{\text{Kitayama, EdS}} = (f(\nu)_{\text{Kitayama}} - f(\nu)_{\text{EdS}}) / f(\nu)_{\text{EdS}}$ where $f(\nu) = \nu f(\nu) / \langle \nu f(\nu) \rangle$.

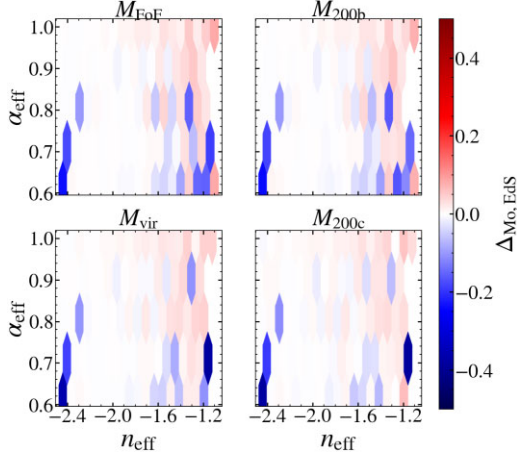


Figure A2. Same as Fig. A1 but for the critical density computed following (Mo, van den Bosch & White 2010).

APPENDIX B: REDSHIFT CORRECTION

For different box sizes, the redshifts of the snapshots vary slightly. This effect is more pronounced at high redshift, where the difference of the output redshifts of different boxes can reach $\Delta z \sim 0.01$. In this time lapse, the mass functions may have evolved, therefore, when combining different box sizes we may be introducing some bias in our data set. The left-hand panel of Fig. B1 displays the expected ratio of the differential mass functions between the output redshifts of the different boxes around $z = 1$. At $M \sim 10^{15} h^{-1} M_{\odot}$, the differences can reach 10 per cent.

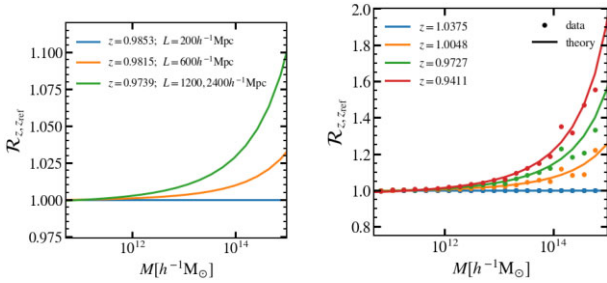


Figure B1. The ratio of the differential mass function between two expansion factors. Left-hand panel: predicted ratios for the output expansion factors corresponding to different box sizes of our simulation set. The reference redshift is $z_{\text{ref}} = 0.9853$. Right-hand panel: predicted and measured ratios for the expansion factors listed in the legend. The reference redshift is $z_{\text{ref}} = 1.0375$.

In order to test whether the predicted evolution of the mass function is accurate, we make use of a simulation presented in Section 6, for which we have many snapshots. In the right-hand panel of Fig. B1, we display the predicted and measured ratios for the redshifts listed in the legend. We can see that the predictions are a good description of the data. For other cosmologies the results are similar.

Thus, we proceed to correct the mass functions of the big box sizes in the following way:

$$\frac{dn}{d \ln M} |_{\text{corrected}}(z_{\text{ref}}) = \frac{dn}{d \ln M} |_{\text{measured}}(z) \times \frac{f(M, z_{\text{ref}})}{f(M, z)}, \quad (\text{B1})$$

where $f(M, z)$ is some model for the differential mass function.

APPENDIX C: EXTENSION TO OTHER MASS DEFINITIONS

In this appendix, we present the main results of our modelling with other mass definitions. These results are analogous to what already described for M_{200b} mass functions.

In general, as seen in Fig. 8, all mass functions show clear correlations with n_{eff} and α_{eff} for a given ν . Therefore, we keep the quadratic and linear functional forms for n_{eff} and α_{eff} in our model (equation 7 and 8), but slightly change the functional form of the peak-height dependence for the different mass definition. For M_{Δ} mass functions, we use the functional form used in Despali et al. (2015) (equation 6). However, the functional form used in Angulo et al. (2012) is more suited to describe M_{FoF} mass functions. Hence, for this mass definition we replace f_1 with

$$\tilde{f}_1(\nu) = A (b \nu^c + 1) \exp(-d \nu^2), \quad (\text{C1})$$

where $\{A, b, c, d\}$ are the free parameters of the ν dependence of our model. By applying the methodology explained in Section 4, we have obtained the best-fitting parameters listed in Tables C1–C3 for M_{FoF} , M_{200c} , and M_{vir} mass functions, respectively.

In Fig. C1, we show the performance of the model for each mass definition. For M_{FoF} mass functions, the residual scatter is consistent with the intrinsic uncertainties of our fit. However, even if the scatter is reduced significantly, for M_{vir} and M_{200c} , the description is not as good as in the other cases. We think that, for both the cases, this may be a consequence of the pseudo-evolution of the boundary definition.

Table C1. A table listing the best-fitting parameters of our M_{FoF} -fitting functions.

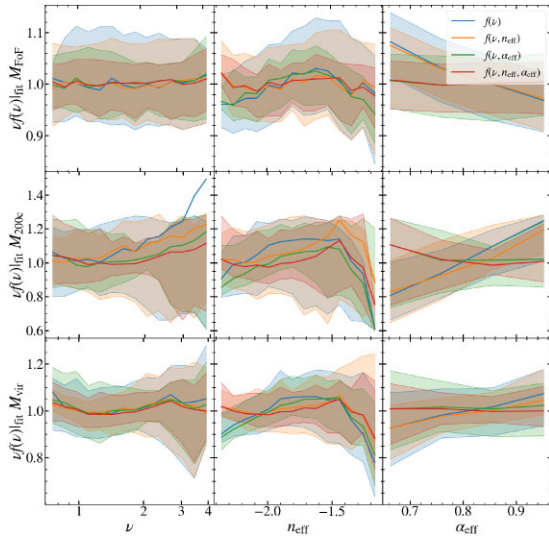
	A	b	c	d	n_0	n_1	n_2	a_0	a_1
$f_1(\nu)$	0.231	1.6871	1.7239	1.1092	–	–	–	–	–
$f_1(\nu)f_2(n_{\text{eff}})$	0.2297	1.6824	1.6437	1.0975	-0.1565	-0.4757	0.6947	–	–
$f_1(\nu)f_3(\alpha_{\text{eff}})$	0.2218	1.8171	1.6643	1.1009	–	–	–	-0.2908	1.2186
$f(\nu, n_{\text{eff}}, \alpha_{\text{eff}})$	0.2276	1.7692	1.6249	1.09	-0.1398	-0.473	0.3671	-0.3715	1.6164

Table C2. A table listing the best-fitting parameters of our M_{200c} -fitting functions.

	a	p	A_{mp}	n_0	n_1	n_2	a_0	a_1
$f_1(\nu)$	0.833	0.1753	0.263	–	–	–	–	–
$f_1(\nu)f_2(n_{\text{eff}})$	0.769	0.2936	0.2314	-0.979	-3.7864	-2.4854	–	–
$f_1(\nu)f_3(\alpha_{\text{eff}})$	0.8186	0.1796	0.2541	–	–	–	–	–
$f(\nu, n_{\text{eff}}, \alpha_{\text{eff}})$	0.7957	0.3069	0.2549	-0.502	-1.79	-0.8305	1.8695	-0.0937

Table C3. A table listing the best-fitting parameters of our M_{vir} -fitting functions.

	a	p	A_{mp}	n_0	n_1	n_2	a_0	a_1
$f_1(\nu)$	0.7814	0.0854	0.3001	–	–	–	–	–
$f_1(\nu)f_2(n_{\text{eff}})$	0.7632	0.1867	0.2939	-0.4999	-1.761	-0.4741	–	–
$f_1(\nu)f_3(\alpha_{\text{eff}})$	0.7793	0.0981	0.2951	–	–	–	0.3581	0.7179
$f(\nu, n_{\text{eff}}, \alpha_{\text{eff}})$	0.7693	0.2074	0.2861	-1.0439	-3.4809	-0.3037	0.1721	0.2899

**Figure C1.** Ratio of the measured mass functions respect to our model. The ratios are displayed against ν , n_{eff} , and α_{eff} values in the columns. In the rows, we show the results for M_{FoF} , M_{200c} , and M_{vir} mass functions.

This paper has been typeset from a $\text{\TeX}/\text{\LaTeX}$ file prepared by the author.